Nanoscale

PAPER

View Article Online
View Journal | View Issue

Check for updates

Cite this: *Nanoscale*, 2023, **15**, 5743

Tuning the electrical properties of graphene oxide through low-temperature thermal annealing†

Cataldo Valentini, [a] Verónica Montes-García, [a] Pietro Antonio Livio,[a] Tomasz Chudziak, [b,c] Jésus Raya,[d] Artur Ciesielski *[a,b] and Paolo Samorì *[a]

Received 31st October 2022,
Accepted 15th February 2023

DOI: 10.1039/d2nr06091d

rsc.li/nanoscale

During the last fifteen years, the reduction of electrically insulating graphene oxide (GO) through the elimination of oxygen containing functional groups and the restoration of sp^2 conjugation yielding its conducting form, known as reduced graphene oxide (rGO), has been widely investigated as a scalable and low-cost method to produce materials featuring graphene-like characteristics. Among various protocols, thermal annealing represents an attractive green approach compatible with industrial processes. However, the high temperatures typically required to accomplish this process are energetically demanding and are incompatible with the use of plastic substrates often desired for flexible electronics applications. Here, we report a systematic study on the low-temperature annealing of GO by optimizing different annealing conditions, *i.e.*, temperature, time, and reduction atmosphere. We show that the reduction is accompanied by structural changes of GO, which affect its electrochemical performance when used as an electrode material in supercapacitors. We demonstrate that thermally-reduced GO (TrGO) obtained under air or inert atmosphere at relatively low temperatures (<300 °C) exhibits low film resistivities (10^{-2}–10^{-4} Ω m) combined with unaltered resistance after 2000 bending cycles when supported on plastic substrates. Moreover, it exhibits enhanced electrochemical characteristics with a specific capacitance of 208 F g^{-1} and a capacitance retention of >99% after 2000 cycles. The reported strategy is an important step forward toward the development of environmentally friendly TrGO for future electrical or electrochemical applications.

Open Access Article. Published on 16 February 2023. Downloaded on 2/15/2026 5:33:27 PM.
This article is licensed under a Creative Commons Attribution 3.0 Unported Licence.

1. Introduction

Graphene oxide (GO) is a unique multifunctional two-dimensional material (2DM) composed of carbon, oxygen, and hydrogen atoms in variable ratios. Firstly synthesized almost 150 years ago,[1] nowadays GO is mainly produced by treating natural graphite flakes with strong oxidants, primarily by making use of the modified Hummers' method.[2] The presence of different oxygenated functional groups (OFGs), such as epoxy, hydroxyl and carbonyl,[3,4] on the basal plane and the edges provides GO with a unique set of mechanical and optical properties along with a good dispersibility and colloidal stability in many solvents, particularly in water.[5–7] In addition, by using well-known chemistry strategies, these OFGs can serve as sites for chemical modification, endowing GO with potential applicability in chemical sensing,[8] solar cells,[9] drug delivery,[10] water desalination[11] or as an active material in energy storage systems (ESSs)[12] among others. Unfortunately, because most of the GO production methods use strong oxidants, such as potassium permanganate, GO possesses a significant number of defects in its crystalline structure. This is concomitant with the loss in electrical conductivity, which limits the direct application of GO in electronics.[13,14] Tremendous efforts have been devoted toward removing OFGs from GO *via* reduction processes with the goal of enhancing the degree of conjugation in the carbon network through the formation of sp^2 species, ultimately boosting the electrical properties of the material aiming at approaching the characteristics of graphene.[15–17] GO reduction yielding electroactive reduced graphene oxide (rGO) can be achieved through a variety of (electro)chemical (CrGO) or thermal (TrGO) methods.[18,19] Chemical reduction is currently the most common and efficient approach for reducing GO using a plethora of reducing agents including hydrazine, sodium borohydride ($NaBH_4$), hydrogen iodide, or L-ascorbic acid.[20–26] However, the price of chemicals, together with the high quantities of generated chemical waste, makes this methodology industrially undesirable.[27] Chemical reagents can be avoided

[a]*Université de Strasbourg and CNRS, ISIS, 8 allée Gaspard Monge, 67000 Strasbourg, France. E-mail: ciesielski@unistra.fr, samori@unistra.fr*
[b]*Centre for Advanced Technologies, Adam Mickiewicz University, Uniwersytetu Poznańskiego 10, 61-614 Poznań, Poland*
[c]*Faculty of Chemistry, Adam Mickiewicz University, Uniwersytetu Poznańskiego 8, 61-614 Poznań, Poland*
[d]*Université de Strasbourg, CNRS, Membrane Biophysics and NMR, Institute of Chemistry, 1 Rue Blaise Pascal, 67000 Strasbourg, France*
† Electronic supplementary information (ESI) available. See DOI: https://doi.org/10.1039/d2nr06091d

Open Access Article. Published on 16 February 2023. Downloaded on 2/15/2026 5:33:27 PM.
This article is licensed under a Creative Commons Attribution 3.0 Unported Licence.

when employing the electrochemical method. In this case, the reduction process relies on the GO-electrode electron exchange, and it can be performed inside an electrochemical cell in the presence of an aqueous buffer solution. Yet, in electrochemical reduction, the deposition and reduction of GO is limited to substrates that can act as electrodes. Even though chemical reduction is one of the most efficient and therefore the most used solution-processed protocols, it is inconvenient as it yields a stoichiometric amount of chemical waste. Therefore, thermal reduction represents one of the most attractive reduction methods due to its low environmental impact. Thermal reduction comprises the annealing of GO under a controlled atmosphere, leading to H_2O, CO_2, and CO as desorption products. It is now well established that under vacuum and annealing temperature ranging between 100 and 185 °C, interlamellar H_2O molecules are desorbed, while epoxide and carbonyl groups are removed between 185–300 °C and 500–700 °C, respectively. In the ranges 700–900 °C and 900–1200 °C ether and hydroxyl groups are removed, leading to a material with a high C/O ratio.[28,29] However, such high temperatures are energetically very demanding and incompatible with GO thermal reduction on plastic substrates for flexible electronics. Typical substrates employed in flexible and wearable electronics, such as polyethyleneterephthalate (PET)[30] and polyimide (PI),[31] retain their mechanical properties at temperatures up to 175 °C and 232 °C, respectively.[30,31] For these reasons, the thermal reduction of GO at relatively low temperatures is highly sought after.

During the last few years, a few works have been reported where the thermal reduction of GO was achieved at relatively low temperatures (<300 °C) (Table S1, ESI†). For instance, it has been found that the reduction temperature can be decreased to 150 °C at atmospheric pressure when GO is dispersed in propylene carbonate as well as in a mixture of water and organic solvents.[32] Grossman *et al.* measured the sheet resistance of GO films annealed at 50 and 80 °C in air. After five days of annealing at 80 °C, the sheet resistance dropped from 10^{10} Ω sq^{-1} of pristine GO to 10^5 Ω sq^{-1} mainly due to the interlamellar H_2O desorption.[33] Chhowalla *et al.* reported that GO films reduced under ultra-high vacuum (UHV) for 15 minutes at 150 and 200 °C have a resistivity of about 10 and 10^{-2} Ω m, respectively, and when the reduction is performed in Ar/H_2 for 15 minutes at 200 °C, a resistivity of 10^{-2} Ω m was obtained.[34]

Thermal reduction in air has been investigated by Nazarov *et al.* in a range of temperatures from 130 to 200 °C with an annealing time of 15 minutes, showing a decrease in resistivity from 4×10^5 Ω m to 4×10^{-2} Ω m. The latter was ascribed to a mechanism comprising first H_2O desorption, followed by OFG desorption releasing CO and CO_2.[35] These last two examples highlight that independently from the reduction atmosphere, when annealing is performed at 200 °C for 15 minutes, the resistivity drops always to ~10^{-2} Ω m. Sun *et al.* studied the kinetics and thermodynamics of GO deoxygenation under argon by thermogravimetric analysis coupled with a mass detector. The CO and CO_2 signals dramatically increased with a temperature near 180 °C, yet traces of CO_2 were already detected at 130 °C.[36] Although these examples prove that GO thermal reduction can be accomplished at relatively low temperatures, the relationship between changes in conductivity with other parameters such as the chemical composition, surface area or crystallinity of TrGO has not yet been elucidated. To the best of our knowledge, there is no systematic study that explores and optimizes the annealing conditions and correlates them with the changes in the GO structure and functions. For instance, as can be seen in Table S1† the reported annealing time has been varied between 15 minutes and 9 days depending on the temperature used. To fill such an important gap, here we report the thermal reduction of GO at different low temperatures (*i.e.*, 100, 130, 150, 200, 250 and 300 °C) under air and inert atmospheres. We investigated the effect of annealing conditions on the chemical structure, various physico-chemical parameters, and the electrochemical performance of the resulting TrGO used as an electrode in a symmetric supercapacitor with a two-electrode system using KOH 6 M as an aqueous electrolyte. Graphene-based materials, such as GO, rGO or high-level oxygen-functionalized GO, have been widely used as active materials in ESS.[37–41] In particular, OFGs endow these materials with a pseudocapacitive nature, making them ideal candidates for supercapacitors. It has been reported that the pseudocapacitance of GO probably comes from electrochemical reactions such as >C–OH ↔ >C═O + H^+ + e^- at the electrode interfaces.[37] For instance, Li *et al.* reported that high-level oxygen-functionalized GO exhibits not only an exceptional supercapacitor performance, reaching a value of specific capacitance as high as 285 F g^{-1} at 1 A g^{-1}, but also a high surfaces area of 512 m^2 g^{-1}.[40] Interestingly, a similar electrochemical performance (capacitance of 264 F g^{-1} at 0.1 A g^{-1}) was achieved for exfoliated graphene, having a much lower density of OGFs.[42] Therefore, not only the presence and density of OFGs are key to achieve a state-of-the-art electrochemical performance, but also other parameters should be carefully controlled. In this work, we investigated the fine tuning of the reduction degree of GO by varying the annealing temperature, time and atmosphere to allow the modulation of the surface area, conductivity and density of electrochemically-active groups, boosting the electrochemical performance of GO. To demonstrate the full compatibility of the reduction strategy with the use of plastic substrates, we fabricated proof-of-concept devices consisting of *ca.* 66 nm thick TrGO films supported on flexible polyethylene terephthalate (PET) substrates and monitored their resistance during 2000 bending cycles.

2. Results and discussion

2.1. Annealing conditions

The thermal reduction of GO under air and N_2 atmospheres was first followed by thermogravimetric analysis (TGA) (Fig. S1, ESI†). The two diagrams show a similar trend, with a first mass loss at 75 °C attributed to interlayer H_2O desorption and a second mass loss at around 200 °C due to CO and CO_2 desorption (Fig. S1, ESI†), achieving a total mass loss of ~45% of

 This journal is © The Royal Society of Chemistry 2023

Open Access Article. Published on 16 February 2023. Downloaded on 2/15/2026 5:33:27 PM.
This article is licensed under a Creative Commons Attribution 3.0 Unported Licence.

the initial weight at 300 °C in agreement with the literature.[33] We then monitored the kinetics of the reduction process by means of TGA with a ramp of 10 °C min^{-1} and an isotherm of 4 hours at 100, 130, 150, 200, 250 and 300 °C (Fig. 1 and S2, ESI†). Interestingly, to the best of our knowledge, TGA kinetic analysis of GO thermal reduction is still unexplored. Under both atmospheres, for 100, 130 and 150 °C, the TrGO weight constantly decreases for 4 hours with a mass loss of about 20, 28 and 35%, respectively. At higher temperatures, the plateau of mass loss (*ca.* 45%) is reached after ~30 minutes. The kinetic analysis at 150 °C is followed up to 24 hours (Fig. S3, ESI†) and the plateau of ~45% mass loss was achieved after 12 hours for both atmospheres. TGA kinetic analysis reveals that 150 and 200 °C are the key threshold temperatures to produce TrGO with a good degree of reduction. However, to gain greater insight into the reduction process, the electrical resistivity is used as an internal gauge by performing thin film conductivity measurements. The films of GO (thickness of 66 ± 11 nm, Fig. S4 and Table S2, ESI†) were annealed at 150 and 200 °C under air and under argon, and the film resistivity was measured at different annealing times with a four-point probe (FPP) to follow the kinetics of the reduction process (Fig. 1b and S5, ESI†). Importantly, N_2 and argon are tested as inert atmospheres (see the Experimental section for details) and no substantial differences in the electrical characteristics are observed on the resulting TrGO. Under air and inert atmospheres (Ar and N_2), the film resistivity gradually decreases upon annealing at 200 °C with the lowest resistivity being achieved after 4 hours (~3×10^{-3} Ω m). At 150 °C under air, the onset of conductivity in TrGO is observed after 4 hours of reduction with the resistivity continuously decreasing even after 24 hours (~3×10^{-2} Ω m). Conversely, when the annealing is performed under argon, the onset of TrGO's conductivity (~2×10^{-1} Ω m) is observed only after 24 hours. To demonstrate the full compatibility of our reduction process with substrates employed in flexible electronics, the annealing of a GO film deposited on polyethylene terephthalate (PET) was performed at 150 °C for 24 h. Then, the mechanical stability of the films was tested by performing 2000 bending cycles (Fig. S6, ESI†). The resistance of the film is constant for the 2000 bending cycles performed with a subtle increase below 1%. Although 24 hours are needed to produce conductive TrGO when the annealing is executed at 150 °C, the reduction time can be reduced to 4 hours when the annealing is performed at temperatures ≥200 °C. Therefore, our subsequent characterization studies were carried out after annealing the samples for 4 hours since the TGA analyses show the plateau achievement for most of the reduction temperatures investigated (Fig. 1a). Fig. 1c shows the room-temperature resistivity of 66 nm thick films of TrGO prepared under air and argon at different annealing temperatures. The resistivity measured for TrGO is above the detection limit of the employed instrument (*i.e.* 10^7 Ω sq^{-1}) for temperatures below 150 °C under argon and below 100 °C under air. Under an argon atmosphere, from 200 °C to 300 °C, the resistivity of TrGO decreases from 3×10^{-3} to 4×10^{-4} Ω m, thereby approaching the resistivity of graphite

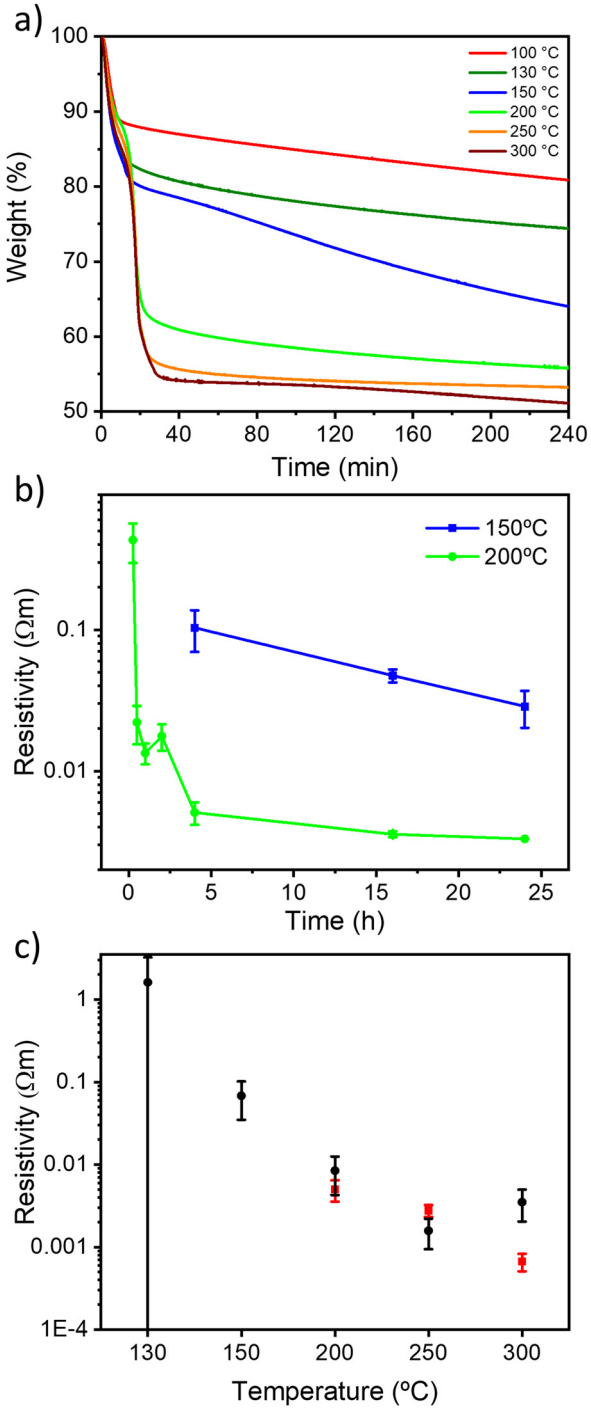

Fig. 1 (a) TGA measurements of weight loss *versus* time for the annealing of GO in air at different temperatures for 4 h, (b) kinetic resistivity measurements for the annealing of GO in air at 150 °C and 200 °C for 24 hours, and (c) resistivity measurements for TrGO in air (black dots) and argon (red dots) for 4 hours.

(10^{-5} Ω m)[43–45] and two orders of magnitude lower than that of rGO annealed at 200 °C in Ar/H_2 or UHV (10^{-2} Ω m).[34] In contrast, the thermal reduction of GO under air shows a constant decrease in film resistivity from 1 Ω m at 130 °C to 10^{-3} Ω m at 250 °C. Conversely, at 300 °C, an increase in the resistivity of

Open Access Article. Published on 16 February 2023. Downloaded on 2/15/2026 5:33:27 PM.
This article is licensed under a Creative Commons Attribution 3.0 Unported Licence.

TrGO is observed, which could be ascribed to the partial oxidation of the GO layers since its ignition temperature is 317 °C.[46] The differences in the kinetics obtained from TGA and the film resistivity measurements may suggest structural reorganization of C_{sp^3}–O to Csp^2–O taking place, which is not accompanied by any weight changes, yet, it determines a transition of the electrical nature of GO from insulating to conductive.

2.2. Compositional, chemical and structural characterization

To gain insight into the chemical composition of TrGO, X-ray photoelectron spectroscopy (XPS) analyses were performed on the GO powders annealed for 4 hours (Fig. 2 and S7–S9, ESI†). From the survey spectra, a C/O ratio of 2.5 is estimated for pristine GO (Fig. S7, ESI†). During the annealing, H_2O, CO and

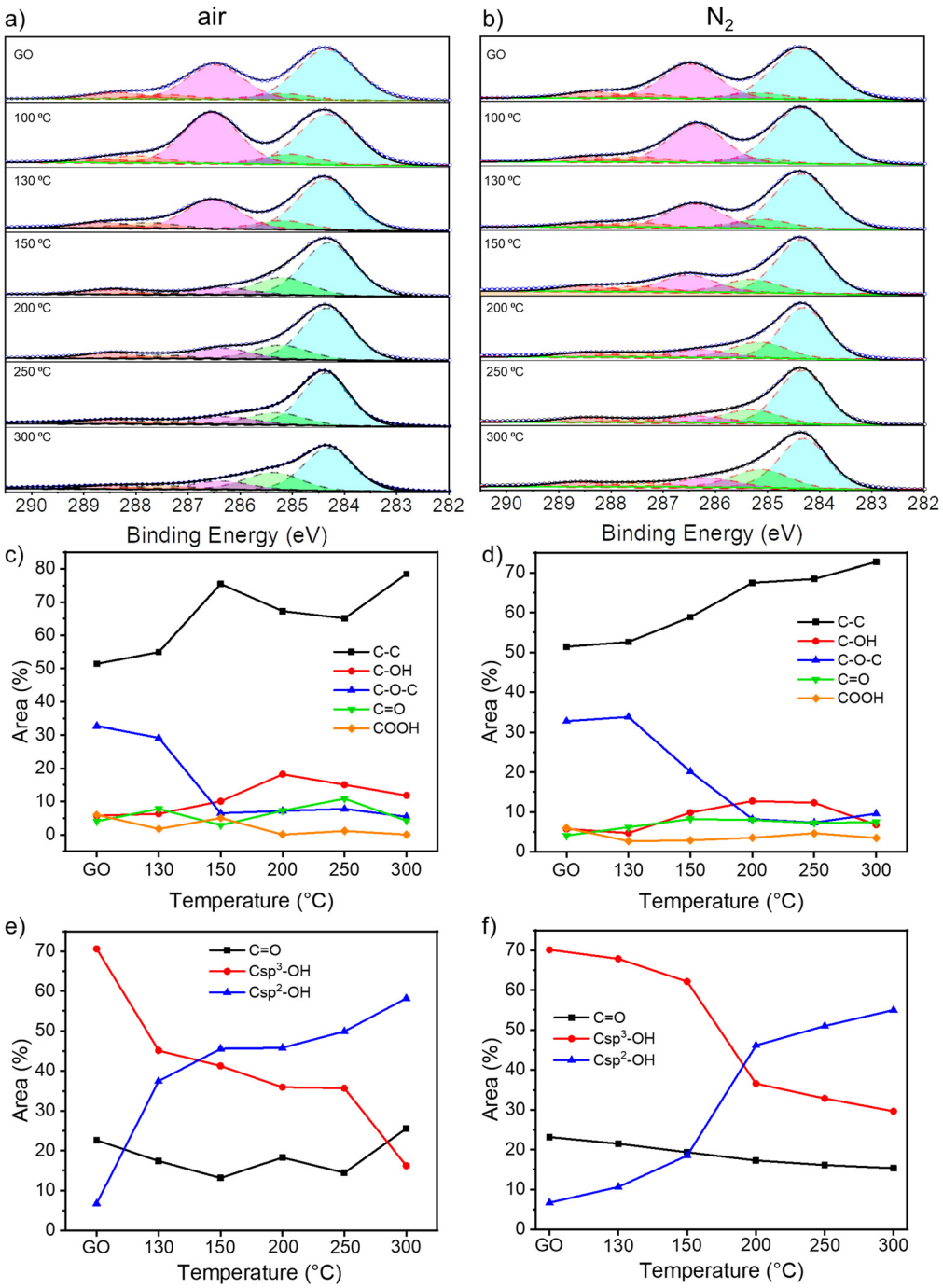

Fig. 2 High-resolution XPS C 1s peaks of thermally reduced GOs under (a) air and (b) N_2; temperature dependence of the relative contribution of C 1s peak components estimated by dividing the area under each component by the whole C 1s peak area for (c) air and (d) N_2; temperature dependence of the relative contribution of O 1s peak components estimated by dividing the area under each component by the whole O 1s peak area for (e) air and (f) N_2.

This journal is © The Royal Society of Chemistry 2023

Open Access Article. Published on 16 February 2023. Downloaded on 2/15/2026 5:33:27 PM.
This article is licensed under a Creative Commons Attribution 3.0 Unported Licence.

CO_2 are released and, consequently, the C/O ratio increases, indicating the reduction process. The C/O ratio increases between 130 and 200 °C for the samples annealed either under air or nitrogen; however, while the C/O ratio increases gradually when the annealing is performed under N_2, more rapid changes are monitored when the annealing is performed in air (Fig. S7, ESI†). For instance, at 150 °C the C/O ratio is 5.05 *versus* 3.40 for TrGO under air and N_2, respectively, indicating that the reduction process at lower temperatures occurs more efficiently in air when compared to the N_2 environment. The high-resolution C 1s spectrum is fitted using 5 Gaussian–Lorentzian curves for the 5 chemical environments: 284.4 eV C–C (C_{sp^2}–C_{sp^2}), 285.15 eV C–O (including C_{sp^2}–O–C_{sp^2}, C_{sp^3}–OH and C_{sp^2}–OH), 286.48 eV C–O–C (C_{sp^3}–O–C_{sp^3}), 287.38 eV C═O, and 288.50 eV COOR (including COOH and lactone) (Fig. 2a and b and S8a, ESI†).[47] Fig. 2c and d show the evolution of the area of each component as a function of annealing temperature. As expected, the area of the C–C peak increases with the annealing temperature under both atmospheres due to the decreasing amount of oxygen in the sample. On the other hand, the area of the C–O–C peak decreases abruptly at 150 °C when annealing is performed under air and at 200 °C when it is performed under N_2. However, the area of the other three peaks remains roughly constant. To gain a greater understanding of the nature of the OFGs, the high-resolution XPS of O 1s spectrum is fitted with 3 Gaussian–Lorentzian curves: 531.08 eV C═O, 532.03 eV C_{sp^3}–O (including C_{sp^3}–O–C_{sp^3}, and C_{sp^3}–OH), and 533.43 eV C_{sp^2}–O (including C_{sp^2}–O–C_{sp^2} and C_{sp^2}–OH) (Fig. S8b and S9, ESI†).[47] Fig. 2e and f show how the relative area of each component varies with the annealing temperature. The area of the C_{sp^3}–OH peak decreases starting from 150 °C when the reduction is performed under air and from 200 °C under N_2, following the same trend as the C–O–C peak. In parallel, the relative area decrement of the C_{sp^3}–O peak is accompanied by a drastic increase in the area of the C_{sp^2}–O peak, indicating the inclusion of oxygen atoms in the conjugated carbon network. From XPS analysis, we can conclude that the threshold temperatures for the thermal reduction of GO under air and N_2 amount to 150 °C and 200 °C, respectively. Further insight into the chemistry of the reduction process was obtained by solid-state NMR magic angle spinning (ssNMR-MAS) analyses (Fig. 3). As previously reported,[48–51] the ssNMR spectrum of GO is deconvoluted in eight curves (Fig. S10, ESI†) corresponding to 60.4 ppm ($^{13}C_{sp^3}$–O–$^{13}C_{sp^3}$), 70.6 ppm ($^{13}C_{sp^3}$–OH), 78.9 ppm ($^{13}C_{sp^3}$–OH, close to defects), 100.2 ppm (^{13}C–OOR), 126.7 ppm ($^{13}C_{sp^2}$–$^{13}C_{sp^2}$), 134.7 ppm ($^{13}C_{sp^2}$–$^{13}C_{sp^2}$ close to defects), 162.4 ppm (C_{sp^2}–O (including C_{sp^2}–O–C_{sp^2} and C_{sp^2}–OH)) and 187.9 ppm (^{13}C═O).[48] In agreement with the XPS analysis, the intensity of peaks related to sp^3 carbons decreases with the increasing annealing temperature, accompanied by the increase of the intensity of sp^2 carbon peaks (Fig. 3c and d). At 150 °C under argon (Fig. 3b and d), a small decrease in the area of $^{13}C_{sp^3}$–O–$^{13}C_{sp^3}$ and $^{13}C_{sp^3}$–O peaks is observed with respect to the pristine GO spectra. However, at 150 °C under air (Fig. 3a and c), these peaks are almost suppressed and the $^{13}C_{sp^2}$–$^{13}C_{sp^2}$ peak arises significantly. The spectra of TrGO at 300 °C under both atmospheres show almost the same profile, the $^{13}C_{sp^2}$–$^{13}C_{sp^2}$ peaks being predominant (Fig. 3a and b). As observed from the XPS analysis, the only OFG formed during the annealing is $^{13}C_{sp^2}$–O and a quantitative evaluation is done by plotting the relative areas of the fitted ssNMR spectra as a function of the reduction temperature (Fig. 3c and d). The $^{13}C_{sp^2}$–O peak increases drastically from 4.7% to 31.2% after the reduction under air at 150 °C and is kept almost constant at 300 °C (27%). However, when the reduction is performed under argon, only at 300 °C the $^{13}C_{sp^2}$–O peak increases sharply to 37%. The generation of $^{13}C_{sp^2}$–O species may be the confirmation of our initial statement where we observed no changes in the weight in the TGA analysis, yet the film resistivity continues to decrease for a certain period of time. In full agreement with the high-resolution XPS, the ssNMR experiments confirm that the reduction of GO can occur at a lower temperature under air when compared to the inert atmosphere.

As previously reported, the features in the Raman spectra of GO and rGO (*i.e.*, band position, intensity ratio, and width) can be related to structural properties such as the oxygen content, crystallinity, and reduction degree of GO.[52–55] The Raman spectra of TrGO are deconvoluted using four Lorentzian curves, which consist of the first-order Raman modes, namely: D, G, D″, and D′ bands (Fig. S11–S14 and Tables S3 and S4, ESI†). The D band, located at 1330–1355 cm^{-1}, arises from the A_{1g} breathing modes of the six-membered rings that are activated by defects such as vacancies, grain boundaries, and disorders in the carbon lattice and the double resonant processes near the K point of the Brillouin zone (BZ) boundary.[55] The G band at 1580–1600 cm^{-1} corresponds to the first-order allowed Raman mode E_{2g}.[52] The additional bands (D′ and D″) arise from the defects present in the graphitic structure of the carbon material. The physical origin of the D′ band at 1610–1620 cm^{-1} is still not fully understood. Some authors have attributed it to the disorder-induced phonon mode due to crystal defects, whereas other authors have attributed this band to the double vacancy corresponding to pentagonal and octagonal rings, usually referred to as 5–8–5 defects.[52] The D″ band at 1500–1550 cm^{-1} is related to the amorphous phase and its intensity is inversely related to the crystallinity.[56] It is well established that the relative intensity of the D band with respect to the G band (I_D/I_G ratio) is an insightful parameter to estimate the degree of defects in the GO derivatives and it has been related to the inverse of the crystallite size on basal planes ($1/L_a$) through the Tuinstra–Koenig model.[57] Upon GO thermal reduction, the intensity of the G peak increases and hence the I_D/I_G ratio decreases with the annealing temperature (Fig. S13, ESI†). The oxygen atomic percentage obtained by XPS is also included in Fig. S13, ESI† for a better understanding of the degree of GO reduction. Fig. S13a, ESI† shows that upon thermal reduction under air, an abrupt decrease of both the I_D/I_G ratio and oxygen atomic percentage at temperatures ≥150 °C is observed, with both parameters becoming stable (I_D/I_G = ~1.42 and ~15% oxygen atoms). However, when the

Open Access Article. Published on 16 February 2023. Downloaded on 2/15/2026 5:33:27 PM.
This article is licensed under a Creative Commons Attribution 3.0 Unported Licence.

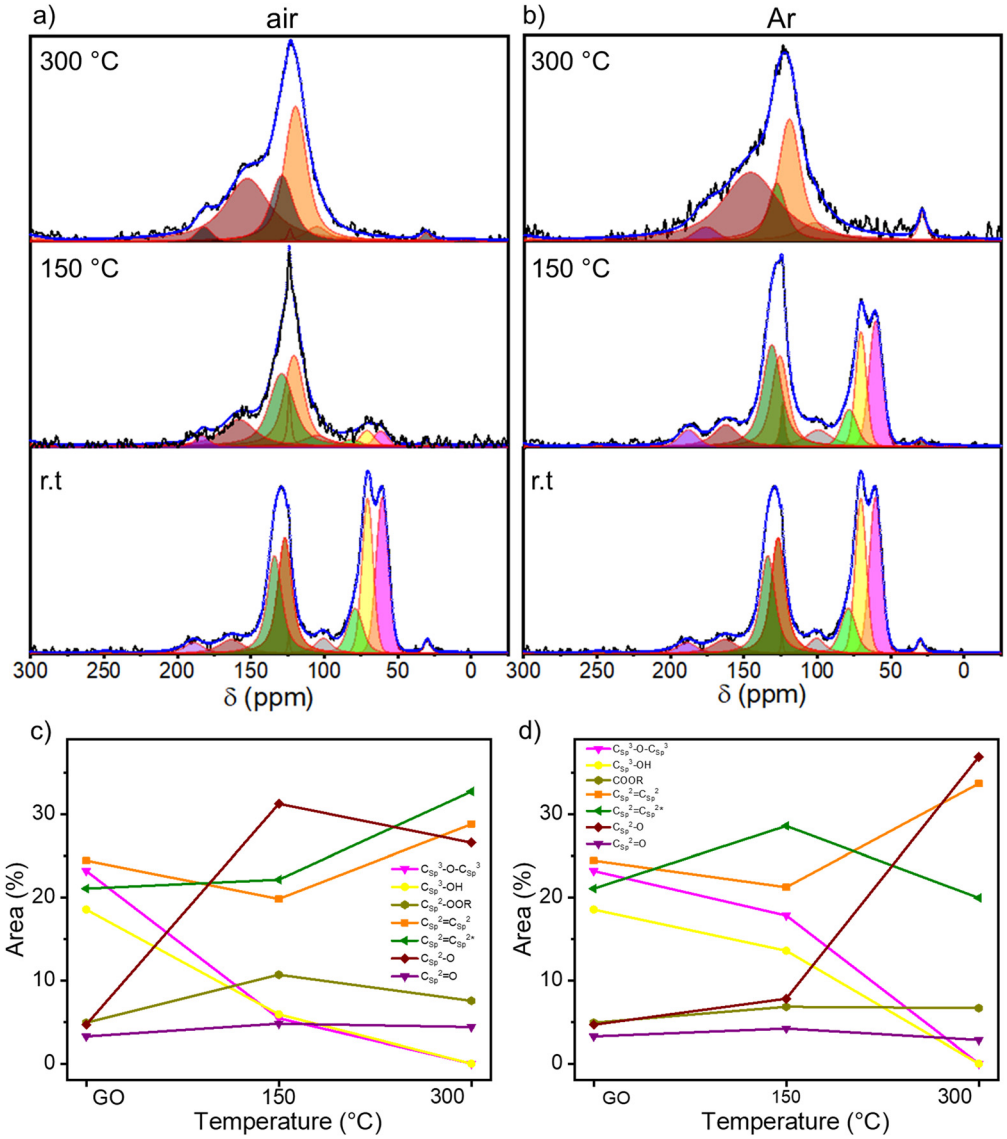

Fig. 3 Solid-state MAS-NMR C 1s spectra of thermally rGO under (a) air and (b) argon; temperature dependence of the relative contribution of NMR spectral components estimated by dividing the area under each component by the whole peak area for (c) air and (d) argon.

thermal reduction is performed under N_2, a more gradual decrease in both parameters is observed, reaching similar minimum values to the reduction under air above 250 °C (Fig. S13b, ESI†). The intensities of the D′ and D″ bands also decrease with the degree of reduction, as the number of defects on the basal plane of GO is lowered. Fig. S14, ESI† shows that the $I_{D'}/I_G$ ratio and the $I_{D''}/I_G$ ratio decrease with the annealing temperature both under air and N_2. It is also important to note that while the $I_{D'}/I_G$ ratio decreased to ~20% of its initial value, the $I_{D''}/I_G$ ratio decreased ~45% (under air) and ~35% (under N_2) of their respective initial values. From this result two conclusions can be drawn: (i) thermal annealing reduces mainly the defects related to the D″ band and (ii) this process is more pronounced for annealing under air, leading to a more crystalline structure.[52,53] The effect of temperature on the crystallinity of TrGO is investigated by powder X-Ray diffraction (PXRD) (Fig. 4 and S14–S16†). Pristine GO diffraction pattern displays one characteristic peak at 2θ = ~11° (peak I) with a full-width half maximum (FWHM) of ~ 1.2° related to the (002) family of planes (Fig. 4a and b).

On the other hand, rGO exhibits one characteristic peak at 2θ = ~25° (peak II) with a larger FWHM of ~5°, five times larger compared to peak I, which indicates a smaller crystallite size.[58] Fig. 4a and b show a gradual disappearance of peak I and a gradual increase of peak II upon increasing the annealing temperature. In agreement with previous characterization studies, such as TGA, XPS and Raman spectroscopy, when the annealing is performed under air, peak II appears at a lower temperature (*i.e.*, 150 °C) compared to annealing performed under argon (*i.e.*, 200 °C), and the full reduction is achieved at 200 °C under both atmospheres. From the PXRD patterns different parameters can be determined (*e.g.*, interlayer dis-

 This journal is © The Royal Society of Chemistry 2023

Open Access Article. Published on 16 February 2023. Downloaded on 2/15/2026 5:33:27 PM.
This article is licensed under a Creative Commons Attribution 3.0 Unported Licence.

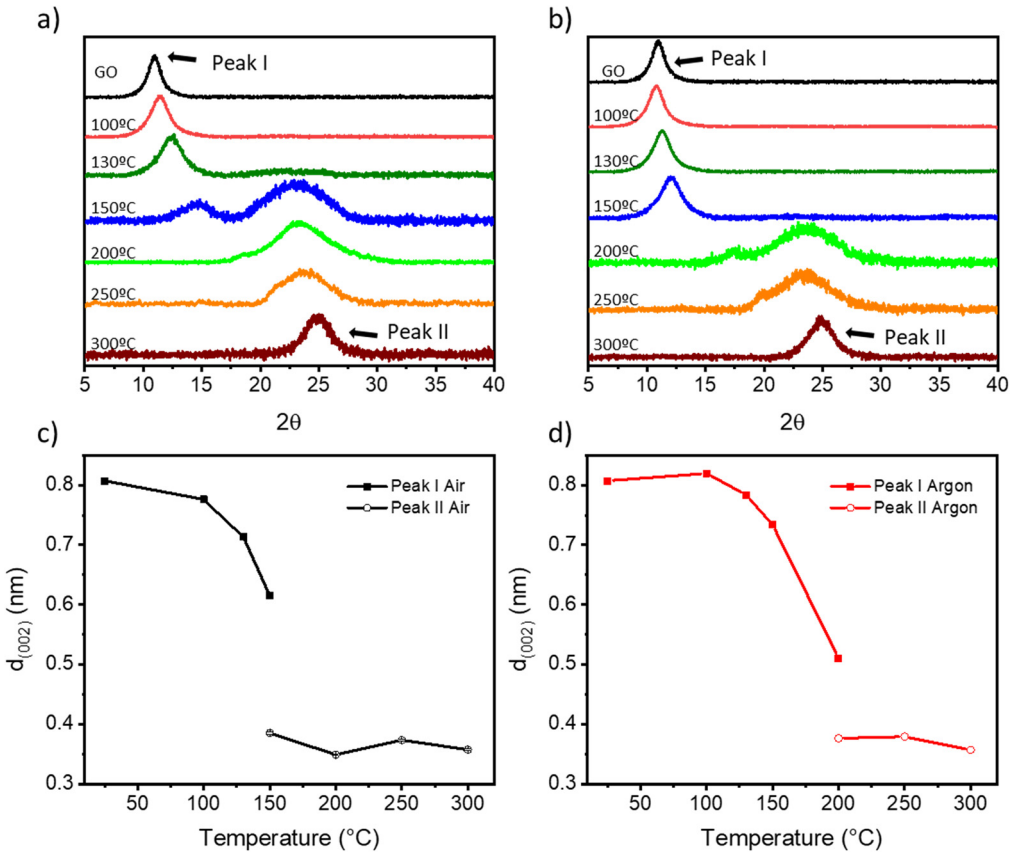

Fig. 4 (a and b) Diffraction patterns of TrGO under (a) air and (b) argon at different temperatures; (c and d) calculated *d*-spacing for peak I (full squares) and peak II (empty circles) for the samples annealed under (c) air and (d) argon.

tance and the number of GO layers) (see the Experimental section for details). First, from the scattering angle (2θ) of each peak (Fig. S15, ESI†), we can quantify the *d*-spacing parameter (Fig. 4c and d). At 150 °C in air and 200 °C in argon, there is the coexistence of peaks I and II, hence two *d*-values are determined. The estimated *d*-spacing of GO is ~0.8 nm, in agreement with the reported values.[52,59] When GO is annealed under air from 100 to 150 °C, peak I shifts toward higher scattering angles, indicating a contraction of the interlayer spacing. This effect can be attributed to the evaporation of the entrapped H_2O. Conversely, when GO is annealed under argon from 100 to 150 °C, only a slight shift of peak I from 11° to 12° is recorded (Fig. 4b). Above 150 °C (under air) and 200 °C (under argon), peak I intensity drops significantly and peak II becomes the major feature in the diffractogram with a calculated *d*-spacing of TrGO of ~0.3 nm.[52,59] The further shrinking of the interlayer distance is related to the partial removal of the OFGs from the GO sheets. Furthermore, considering the crystallite size (L_c) (Fig. S16, ESI†) and the interlayer spacing *d* (002) (Fig. 4c and d), we estimated the theoretical number of (r)GO sheets per crystallite domain (Fig. S17, ESI†). Our results clearly show that for GO annealed in air few layer-thick rGO sheets (4–6 layers) can be produced already at 150 °C. Remarkably, the low-temperature annealing under both atmospheres (*i.e.*, air and argon) allows us to produce high-quality few-layer rGO, starting from commercially available GO with a high percentage of monolayers (>95%) with promising characteristics for integration into electronic devices. The porosity of (Tr)GO annealed at different temperatures under air or argon is evaluated by recording N_2 adsorption–desorption isotherms at 77 K (Fig. S18 and Table S5, ESI†). The adsorption isotherms of TrGO exhibited type-I sorption isotherms, with steep rises appearing at a low relative pressure and type-IV sorption features with adsorption/desorption hysteresis at higher pressure. The calculated Brunauer–Emmett–Teller (BET) surface area of TrGO increases gradually with the rising annealing temperature up to 300 °C, from 12.61 $m^2\ g^{-1}$ for the as-prepared GO to 480.44 $m^2\ g^{-1}$, when the annealing is performed under air. In contrast, when the annealing is performed under argon the surface area abruptly increases at 200 °C to 439.92 $m^2\ g^{-1}$, and then remains roughly constant. The average pore size increases gradually with thermal treatment temperature, following the same tendency as the specific surface area (Table S5, ESI†). Fig. S18c and d, ESI† show the differential distribution of pore volumes *versus* pore sizes for TrGO under (S18c†) air and (S18d†) argon. It reveals that all materials have a predominant mesopore distribution with sizes in the range between 10 and 100 nm. The work function of (Tr)GO was calculated by photoelectron yield spectroscopy in air (PYSA) (Fig. S19, ESI†). The work function of GO (5.59 ± 0.03 eV) decreases gradually with

Open Access Article. Published on 16 February 2023. Downloaded on 2/15/2026 5:33:27 PM.
This article is licensed under a Creative Commons Attribution 3.0 Unported Licence.

the increase in the annealing temperature under both atmospheres until reaching a stable value of ~5.14 eV.

2.3. Electrochemical characterization

The electrochemical properties of all the GO samples were evaluated in a symmetrical two-electrode cell by cyclic voltammetry (CV), galvanostatic charge/discharge (GCD) and electrochemical impedance spectroscopy (EIS). Fig. 5a and d show the cyclic voltammograms of GO thermally reduced under (a) air and under (d) argon using a 6 M KOH aqueous electrolyte between 0 and 0.6 V at a scan rate of 50 mV s^{-1}. The CV curves of TrGO show a quasi-rectangular shape, indicating the pseudocapacitive nature of (Tr)GO.[37] When the reduction is performed under air, the transition from GO to TrGO is gradual, starting at 130 °C but reaching an actual quasi-rectangular shape from 150 °C. The area of the CV curve increases with the temperature of annealing up to 200 °C. Above 250 °C, the voltammogram starts to contract slightly, which is attributed to the initiation of the combustion of the material, as demonstrated by TGA and film resistivity measurements. Interestingly, when the reduction is performed under argon there are only two clear states of reduction. At 200 °C the area of the CV curves abruptly increases, and above this temperature, the CV curves became stable. Rate capability is also an important feature for energy storage devices. The CV curves for GO (Fig. S20, ESI†) and TrGO under air (Fig. S21, ESI†) and under argon (Fig. S22, ESI†) at different scan rates were obtained. When GO is annealed above 150 °C or 200 °C under air or argon, respectively, the cyclic voltammograms remain in box-like shapes with a little deviation at lower potentials, even when the scan rate increases to 200 mV s^{-1}, implying a quick charge propagation and hence a good rate capability.[42] On the other hand, the CV curves of GO and GO annealed below 150 °C or 200 °C under air or argon respectively deviate from the ideal box-shape, indicating that the device is being overcharged, as a result of the poor material conductivity as well as the occurrence of parasitic side reactions, such as decomposition of the electrode material, the electrolyte, or a combination of both.[60] This finding is in full agreement with the film resistivity analysis.

The pseudocapacitive behaviour of TrGO under two different atmospheres is confirmed by galvanostatic charge/discharge curves, as shown in Fig. 5b and e. The voltage–time curve exhibits a quasi-linear shape under both atmospheres and similar trends to those obtained by CV. The specific capacitances of TrGO were calculated from GCD curves at different current densities, as can be seen in Fig. S23 and S24, ESI† (see the Experimental section for calculation details). With an increase of the current density, the capacitances of GO and TrGO decrease very slowly under both atmospheres, indicating, in agreement with CV at different scan rates, that (Tr)GO has excellent rate capability. The maximum specific capacitance for TrGO reduced under air amounts to 154.8 ± 5.4 F g^{-1} at a current density of 0.1 A g^{-1} (Fig. S24, ESI†) for samples reduced at 200 °C. On the other hand, the maximum value observed under argon is slightly higher 173.5 ± 12.6 F g^{-1} at a current density of 0.1 A g^{-1} (Fig. S24, ESI†) at 300 °C. These values represent an outstanding 60-fold increase when compared to the initial capacitance of GO (~2.5 F g^{-1}). The values of specific capacitance measured for TrGO are similar

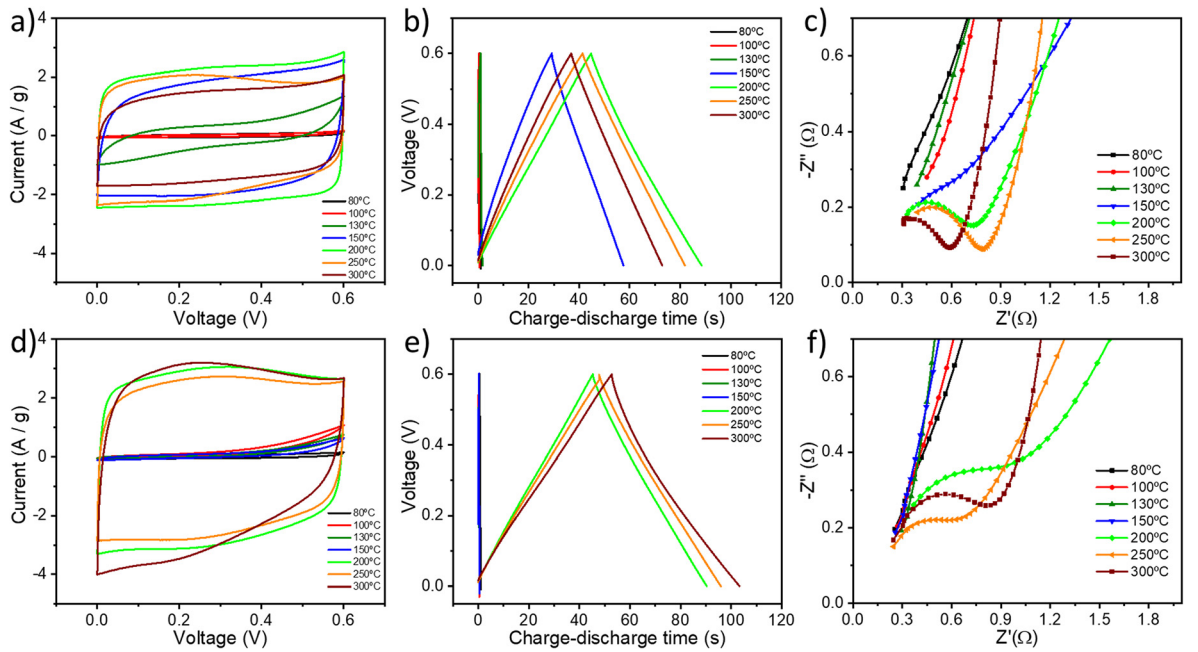

Fig. 5 Electrochemical characterization of thermally reduced GO at different temperatures under (a–c) air and under (d–f) argon. (a and d) CV curves at a scan rate of 50 mV s^{-1}. (b and e) GCD curves at a current density of 1 A g^{-1}. (c and f) Magnification of the high-frequency region of the Nyquist plots.

 This journal is © The Royal Society of Chemistry 2023

Open Access Article. Published on 16 February 2023. Downloaded on 2/15/2026 5:33:27 PM.
This article is licensed under a Creative Commons Attribution 3.0 Unported Licence.

using 1 M H_2SO_4 and 6 M KOH as aqueous electrolytes (Fig. S25, ESI†).[61]

The evolution of the specific capacitance values as a function of the annealing temperature can result from three different contributions. First, the increase in surface area with the annealing temperature (Fig. S26a and c, ESI†) is directly proportional to the electrochemical performance. The surface area of pristine GO (~13 m^2 g^{-1}) increases up to 40 times (~480 m^2 g^{-1}) upon thermal annealing under both atmospheres due to the gradual removal of OFGs. However, it has been reported that the GO annealing at higher temperatures (≥500–800 °C) would lead to a decrease in surface area, which is due to the partial coalescence and overlap of graphene sheets.[62–64] In the present case, we observed this phenomenon starting at a temperature of 300 °C, with the crystallite dimension obtained from XRD. Therefore, the largest surface area is achieved at low annealing temperatures (<300 °C). Secondly, it is also important to highlight that the presence of heteroatoms and functional groups is advantageous, as they can provide a large additional pseudocapacitance.[37] Interestingly, Zhao *et al.* showed that the annealing of GO at temperatures between 200 and 500 °C can lead to materials with higher surface area and the specific capacitance exhibited a decrease from 200 °C due to the high loss of OFGs.[62] As evidenced by XPS and ssNMR analyses, GO samples annealed at a temperature <300 °C feature small amounts of OFGs, in particular C_{sp^2}–O, which seem to be the key for the enhanced electrochemical performance of TrGO. Lastly, film conductivity also plays a key role in the electrochemical performance as low resistivity guarantees a quick charge propagation through the electrode material. In the present case, as we are removing OFGs, the mechanism is governed by the increase in the surface area of the GO and the increase in film conductivity (Fig. S26b and d, ESI†), yielding capacitance values comparable to the state of the art of TrGO (Table S6, ESI†).[42,62,63,65–68] When the reduction is performed under argon, the increase in specific capacitance with the annealing temperature is followed by the increase in both surface area and film conductivity. Differently, when the reduction is carried out under air the same trend also occurs for the specific capacitance and film conductivity but not for the surface area at 150 and 200 °C. We can conclude that the increase in film conductivity has a higher effect on the electrochemical performance of TrGO under air, while under argon the effect of surface area and film conductivity cannot be distinguished. Importantly, a high annealing temperature (>300 °C, independently from the reduction atmosphere) is detrimental for the electrochemical performance of TrGO. The TrGO samples prepared under such conditions feature a smaller surface area and decreased pseudocapacitance due to the reduction of OFGs on GO's surface. Furthermore, an increase in the interface electrical resistance arises from the overlap of graphene sheets. By employing the mildest and optimized annealing conditions, our TrGO exhibits state of the art capacitance (Table S6, ESI†) compared to other TrGO prepared at low temperatures. The device's electrochemical performance depends on its individual components, which are the electrode, electrolyte, separator and current collector.[69] Although the charges are mainly stored in the electrode material (*i.e.*, TrGO), the other components also play key roles in the overall electrochemical performance.[70] The influence of the current collector is tested by comparing carbon paper with Ni foam. As can be seen in Fig. S27, ESI† the specific capacitance of thermally reduced GO at 200 °C under air and 6 M KOH as an electrolyte increases from 154 F g^{-1} to 208 F g^{-1} at 0.1 A g^{-1} current density using a Ni foam current collector. This increase originates from the higher electrical conductivity of the Ni foam current collector as well as the stability of the whole system at higher voltages (up to 1 V), as can be seen in Fig. S27b and c, ESI.† Furthermore, the electrochemical impedance spectroscopy data are analysed using Nyquist and Bode plots (Fig. 5c and f and S28, ESI†). The Nyquist plot of an ideal double-layer capacitor should be a vertical line, parallel to the imaginary axis.[71] The presence of a semicircle at high frequencies is related to the different OFGs on the GO surface endowing it with a pseudocapacitive behavior. For GO and TrGO under air up to 130 °C and up to 150 °C under argon, no semicircle can be observed (Fig. 5c and f and S28a and d, ESI†) due to the intrinsic internal resistance of the electrode materials being too high as has been shown in the film resistivity analysis (Fig. 1c). The experimental results are well fitted with the two indicated circuits (Scheme S1†). R_s is the combined internal resistance, including the interfacial contact resistance of the material with the current collector, the ohmic resistance of the electrolyte and the intrinsic resistance of the current collector, which can be obtained from the high-frequency region of the Nyquist plot at the intersection on the real axis.[72] R_{ct} is the interfacial charge transfer resistance, corresponding to the diameter of the semicircle, which represents the resistance of electrochemical reactions at the electrode surface.[73] Furthermore, the semicircle can also reflect a constant phase element (CPE) due to the double-layer behaviour. In the middle frequency region, the sloping transmission line corresponds to the Warburg element Z_W, describing the transfer and diffusion of the electrons and electrolyte ions in the pores of the electrode materials. The nearly vertical line in the low frequency region reflects an excellent capacitive behaviour of the electrodes. The fitting parameters can be seen in Table S7, ESI.† The low R_{ct} values are consistent with the fact that at a scanning rate as high as 200 mV s^{-1}, the CV curve still shows a rectangular shape with small distortion, indicating that the TrGO samples show a good rate capability.

From the Nyquist and Bode plots an important parameter can be calculated, the conductance of the (Tr)GO film (G_p) (see the Experimental section for details), which can be converted to conductivity when normalized by the film thickness. Fig. S29a, ESI† shows the G_p of (Tr)GO under air at different temperatures in the frequency range of 0.1–10^6 Hz. From 0.1–10 Hz, there is no dependence of the annealing temperature and G_p, and from 10^4–10^6 Hz G_p is not stable. Therefore, for a better comparison, the frequency range of 10–10^4 Hz is selected. Fig. S29b and c, ESI† show the G_p of (Tr)GO under air (Fig. S29b†) and under argon (Fig. S29c†) at different tempera-

Open Access Article. Published on 16 February 2023. Downloaded on 2/15/2026 5:33:27 PM.
This article is licensed under a Creative Commons Attribution 3.0 Unported Licence.

tures. The same trend, in full agreement with previous characterization techniques, is obtained. When the annealing is performed under air, Gp gradually increases from 150 °C with the annealing temperature. Differently, when the annealing is performed under argon, Gp increases abruptly at 200 °C and then becomes constant at higher annealing temperatures. In all cases, the film thickness is ~1 mm and the conductivity plot (Fig. S30, ESI†) exhibits similar values compared to the ones obtained from film resistance measurements (Fig. 1c, S26b and d, ESI†). The energy and power densities of TrGO annealed at 200 °C under air are plotted in Fig. S31, ESI† with: (1) the highest energy density of 7.35 W h kg^{-1} achieved at a power density of 0.057 kW kg^{-1} and (2) the highest power density of 2.86 kW kg^{-1} achieved at an energy density of 6.62 W h kg^{-1}. These values of energy and power densities are well suited for energy storage applications[74] Finally, to investigate the electrochemical stability of TrGO at 200 °C under air, GCD cycling was performed at a current density of 3 A g^{-1} (Fig. S32, ESI†). After 2000 cycles, the capacitance decay is only 0.4%, indicating that TrGO has excellent cycle durability.

3. Conclusions

In summary, we presented an optimized, scalable, easily controllable, and low-temperature (<300 °C) annealing procedure without chemical treatments for the production of reduced graphene oxide with electrical properties at will. The use of multiple techniques made it possible to gain an unprecedented insight and control over the compositional, structural, morphological and (electro)chemical characteristics of the materials. The oxygen atoms' reorganization on the GO surface to promote H_2O and CO_2 release is favoured in a range of temperatures between 130 and 200 °C as shown from the TGA, XPS and ssNMR analyses. Therefore, it is possible to achieve the elimination of OFGs without promoting the ignition of the carbon framework when the reduction is performed in air. The main OFG formed during the annealing is C_{sp^2}–O, which does not result in any mass loss but it determines a variation of the electrical nature of GO from insulating to conductive. We have demonstrated that film resistivities of ~10^{-2}–10^{-4} Ω m can be achieved by annealing under air between 150 and 200 °C for 24 and 4 hours, respectively, and under an inert atmosphere from 200 °C for 4 hours. Such results indicate the viability of GO reduction upon annealing at temperatures as low as 150 °C, compatible with the use of plastic substrates. Interestingly, films supported on plastic substrates showed unaltered resistance when subjected to 2000 bending cycles. This represents an important step forward for application in wearable and flexible electronics. Thermally-reduced GO at 200 °C under air exhibited an enhanced electrochemical performance (a specific capacitance of 208 F g^{-1} at a current density of 0.1 A g^{-1} and a capacitance retention >99% after 2000 cycles). Although the loss of OFGs is detrimental to the electrochemical performance, it is compensated with a high gain in the surface area and film conductivity, yielding ~450 m^2 g^{-1} and 10^3 S m^{-1}, respectively. Our protocol can be performed in any lab and it is scalable for industrial applications.

4. Experimental section

4.1. Materials

Graphene oxide (GO, 4 mg mL^{-1}, monolayer content >95%, Graphenea), polytetrafluoroethylene (PTFE) binder (Sigma Aldrich), *N*-methyl-2-pyrrolidone (NMP) (Sigma Aldrich), potassium hydroxide (KOH) (Fisher), sulfuric acid (H_2SO_4) (Sigma Aldrich), tetraethylammonium tetrafluoroborate ($(C_2H_5)_4NBF_4$) (Acros Organics), and acetonitrile (Carlo Erba reagents).

GO (powder). Solid GO was obtained by lyophilization from the commercially available GO solution using a freeze dryer (Christ).

GO films. A 4 mg mL^{-1} aqueous dispersion of GO was diluted to a concentration of 0.4 mg mL^{-1}, then drop-cast on glass slides, and finally dried under air.

4.2. Methods

Thermal annealing of GO. GO (powder) and GO films were annealed at different temperatures for 4 or 24 h in a muffle oven (16 cm × 16 cm) under air (1 bar) or in a tubular oven (100 cm × 7 cm) under argon (continuous flow 1 bar) before the measurements. GO powders were annealed from a mg scale to a gram scale. Besides, GO (powder) was also annealed at different temperatures for 4 or 24 h in a thermogravimetric analyzer (TGA) under air or nitrogen before the Raman and X-ray photoelectron spectroscopy (XPS) analyses. The composition, structure, and texture properties of the materials were investigated by powder X-ray powder diffraction (PXRD) measurements (Bruker D8 X-ray diffractometer). TGA decomposition curves were recorded in the range of 25–300 °C operating under air or a nitrogen atmosphere with a thermal step of 10 °C min^{-1} on a Mettler Toledo TGA/SDTA851e system. An XPS (Thermo Scientific K-Alpha X-ray photoelectron spectrometer) equipped with an aluminium X-ray source (energy 1.4866 keV) at a vacuum level of 10^{-8}–10^{-9} mbar in the main chamber was used. The spot size of the X-ray beam was fixed at 400 μm. Raman spectra were acquired with a Renishaw inVia Reflex system. The spectrograph used a high-resolution grating (2400 grooves per cm) with additional bandpass filter optics, a confocal microscope, and a 2D-CCD camera. Excitation was carried out using a 532 nm laser excitation beam with a 100× objective, 0.2 mW maximum power and 1 s acquisition time. The specific surface area was measured using a Micromeritics ASAP 2050 surface area and porosity analyzer. Before the Brunauer–Emmett–Teller (BET) measurements, the samples were outgassed for 12 hours at 95 °C. Adsorption isotherms were calculated for nitrogen adsorption at 77 K and a pressure up to 1 bar. Photoelectron yield spectroscopy in air (PYSA) measurements were performed on (Tr)GO drop-cast on an ITO/glass substrate with an AC-2 photoelectron spectrometer

 This journal is © The Royal Society of Chemistry 2023

Open Access Article. Published on 16 February 2023. Downloaded on 2/15/2026 5:33:27 PM.
This article is licensed under a Creative Commons Attribution 3.0 Unported Licence.

(Riken-Keiki Co.). A UV light intensity of 40 nW and a counting time of 10 seconds per point were used for the measurement.

4.3. Solid-state MAS NMR

All experiments were performed at room temperature on an AVANCE 500 MHz wide bore spectrometer (Bruker™) operating at a frequency of 500.12 MHz for ^{1}H NMR and 188.5 MHz for ^{13}C NMR. As GO is generally barely protonated the classical cross-polarization magic angle spinning (CP/MAS) proves ineffective in obtaining ^{13}C quantitatively,[75] Then a DP/MAS (direct polarization with magic angle spinning) pulse scheme was preferred by using a speed synchronized spin echo sequence with proton decoupling during acquisition.[76] The latter allows us to obtain undistorted line shapes and filter out background probe signals, giving integrable spectra providing recycling delays that fulfill quantitative rules, *i.e.* equal to *ca.* 3 to 5 times that of the longitudinal relaxation time (^{13}C T_1). Under our conditions (speed and fields) T_1s were measured to be less than 300 ms (saturation/recovery method, data not shown). ^{13}C spectra were recorded using a triple resonance MAS probe (Bruker™), allowing the samples to be spun at 22.5 kHz after packing them inside 3.2 mm o.d. zirconia rotors (closed with Vespel caps). Recycle-time delays were set to 1.5 seconds and 10 240 transients over 8192 time-domain points separated by 2 μs dwell time were added, leading to a 61.035156 Hz pt^{-1} spectral resolution (spectral width = 250 kHz and total acquisition time per spectrum = 4 hours 30 min). ^{13}C NMR and ^{1}H NMR RF-fields were 60 kHz and 95 kHz, respectively. For the 300 °C thermally treated samples, the conductivity was such that it was very difficult to tune the probe. The concern was fixed by dispersing these powders in silica.[77] Raw data were processed with a 150 Hz Lorentzian filter followed by Fourier transformation without zero filling. Chemical shifts are referenced to TMS by the substitution method using adamantane as an external reference. Spectral deconvolution was performed within Topspin™ software suite from Bruker™ using a CSA (chemical shift anisotropy) model.

4.4. Four-point probe measurements

Film resistivities were measured with a Jandel probe, Model RM3000, and the limit of detection is 10^7 Ω sq^{-1}. The resistivity (ρ) was obtained using the following equation:

$$\rho = R_s \cdot l \quad (1)$$

where R_s is the sheet resistance and l is the thickness of the film.

4.5. Atomic force microscopy (AFM)

AFM characterization was carried out to determine the GO film thickness using a Bruker Dimension Icon microscope in intermittent contact mode using a TESPA-V2 silicon tip with a force constant (k) = 42 N m^{-1}.

4.6. Bending characterization

GO water solution (0.4 mg mL^{-1}) was spray coated onto PET substrates at 100 °C (2.5 × 1.2 cm^2, 125 μm thick) and annealed at 150 °C for 24 h in air. The reduced film of GO on PET was allowed to contact electrically with conductive copper tape. The sheet resistance of the film was 40 kΩ sq^{-1}. The stability test of the TrGO conductive film to fatigue bending was carried out by performing 2000 bending cycles with a bending radius of 6 mm using a digital force gauge (Mark-10, M7-025E, ~25 N) equipped with a motorized test stand (Mark-10, ESM-S-8 303E). All the above-mentioned tests were performed by applying a bias voltage of 1 V by means of a Keithley 2635B.

4.7. Fabrication of supercapacitors

The electrochemical performance of thermally-reduced graphene oxide was measured in a two-electrode symmetric supercapacitor system. Two electrodes were assembled in CR2032 stainless steel coin-type cells with a porous cellulose membrane as a separator and 6 M KOH or 1 M H_2SO_4 aqueous solution or 1 M tetraethylammonium tetrafluoroborate ($(C_2H_5)_4NBF_4$) in acetonitrile as an electrolyte. The preparation procedure of the electrodes is shown as follows. First, a paste was prepared by fully mixing 90 wt% of sample (18 mg), 10 wt% polytetrafluoroethylene (PTFE) binder (2 mg) and a certain amount of *N*-methyl-2-pyrrolidone (NMP) using an agate mortar and pestle. The paste was coated over the carbon paper or Ni foam electrode, which was then subjected to a quick dry at 80 °C. The electrodes were completely dried at 80 °C in a vacuum oven for 16 h. Finally, the Ni foam electrodes were pressed at 10 MPa for 1 minute. The mass loading of (thermally reduced) graphene oxide was ~0.5 mg in each electrode.

The devices were electrically characterized by cyclic voltammetry (CV), galvanostatic charge/discharge (GCD), and electrochemical impedance spectroscopy (EIS) using a Metrohm Autolab PGSTAT204 potentiostat/galvanostat and the Autolab DuoCoin cell holder (Metrohm AG). The frequency range for the impedance spectra was from 0.1 Hz to 100 kHz with a sine-wave voltage signal amplitude of 50 mV (root mean square, RMS). CV and GCD tests were carried out between 0 and 0.6 V. Stability tests were performed using a battery testing system (Neware).

4.8. Calculation of the specific capacitances, energy densities and power densities

From charge–discharge measurements, the specific capacitances (C_p), energy densities (E), and power densities (P) of (thermally reduced) graphene oxide were obtained from the acquired data using the following equations:[78]

$$C_p = \frac{2 \cdot I \cdot \Delta t}{m \cdot \Delta V} \quad (2)$$

$$E = \frac{1}{2} \cdot C_p \cdot \Delta V^2 \quad (3)$$

$$P = \frac{E}{\Delta t} \quad (4)$$

where I is the discharge current (A), Δt is the discharge time (s), m is the weight of the active material in an individual electrode (g), and ΔV is the discharge voltage (V) excluding the internal resistance (iR) drop during the discharge process.

Open Access Article. Published on 16 February 2023. Downloaded on 2/15/2026 5:33:27 PM.
This article is licensed under a Creative Commons Attribution 3.0 Unported Licence.

4.9. Calculation of conductance (G_p)

As previously reported,[79] we can express the sample G_p in terms of the measurable, fundamental Z-related parameters:

$$G_p = \frac{Z'}{|Z|^2} \quad (5)$$

where Z' is the real part of the impedance obtained from the Nyquist plot and Z is the modulus of the impedance obtained from the Bode plot.

Conflicts of interest

There are no conflicts to declare.

Acknowledgements

We acknowledge the funding from the European Commission through the ERC project SUPRA2DMAT (GA-833707), the Graphene Flagship Core 3 project (GA-881603) and the Marie Sklodowska Curie ETN project BORGES (GA-813863), as well as the Agence Nationale de la Recherche through the Interdisciplinary Thematic Institute SysChem *via* the IdEx Unistra (ANR-10-IDEX-0002) within the program Investissement d'Avenir, the International Center for Frontier Research in Chemistry (icFRC), the Institut Universitaire de France (IUF), and the National Science Centre, Poland (grant no. 2019/35/B/ST5/01568 and 2021/41/N/ST5/01112).

References

1 A. K. Geim, *Phys. Scr.*, 2012, **T146**, 014003.
2 W. S. Hummers and R. E. Offeman, *J. Am. Chem. Soc.*, 1958, **80**, 1339–1339.
3 J. Guerrero-Contreras and F. Caballero-Briones, *Mater. Chem. Phys.*, 2015, **153**, 209–220.
4 N. I. Zaaba, K. L. Foo, U. Hashim, S. J. Tan, W.-W. Liu and C. H. Voon, *Procedia Eng.*, 2017, **184**, 469–477.
5 D. Chen, H. Feng and J. Li, *Chem. Rev.*, 2012, **112**, 6027–6053.
6 V. Agarwal and P. B. Zetterlund, *Chem. Eng. J.*, 2021, **405**, 127018.
7 J. W. Suk, R. D. Piner, J. An and R. S. Ruoff, *ACS Nano*, 2010, **4**, 6557–6564.
8 C. Anichini, W. Czepa, D. Pakulski, A. Aliprandi, A. Ciesielski and P. Samorì, *Chem. Soc. Rev.*, 2018, **47**, 4860–4908.
9 Y. Song, X. Li, C. Mackin, X. Zhang, W. Fang, T. Palacios, H. Zhu and J. Kong, *Nano Lett.*, 2015, **15**, 2104–2110.
10 J. Liu, L. Cui and D. Losic, *Acta Biomater.*, 2013, **9**, 9243–9257.
11 D. Pakulski, A. Gorczyński, D. Marcinkowski, W. Czepa, T. Chudziak, S. Witomska, Y. Nishina, V. Patroniak, A. Ciesielski and P. Samorì, *Nanoscale*, 2021, **13**, 10490–10499.
12 S. Witomska, Z. Liu, W. Czepa, A. Aliprandi, D. Pakulski, P. Pawluć, A. Ciesielski and P. Samorì, *J. Am. Chem. Soc.*, 2019, **141**, 482–487.
13 Y. Zhu, S. Murali, W. Cai, X. Li, J. W. Suk, J. R. Potts and R. S. Ruoff, *Adv. Mater.*, 2010, **22**, 3906–3924.
14 G. Eda and M. Chhowalla, *Adv. Mater.*, 2010, **22**, 2392–2415.
15 A. Ciesielski and P. Samorì, *Chem. Soc. Rev.*, 2014, **43**, 381–398.
16 X. Zhang, L. Hou, A. Ciesielski and P. Samorì, *Adv. Energy Mater.*, 2016, **6**, 1600671.
17 A. K. Geim and K. S. Novoselov, *Nat. Mater.*, 2007, **6**, 183–191.
18 J. J. Xingfa Gao and S. Nagase, *J. Phys. Chem. C*, 2010, **114**, 832–842.
19 Y. Shao, J. Wang, M. Engelhard, C. Wang and Y. Lin, *J. Mater. Chem.*, 2010, **20**, 743–748.
20 L. G. Guex, B. Sacchi, K. F. Peuvot, R. L. Andersson, A. M. Pourrahimi, V. Strom, S. Farris and R. T. Olsson, *Nanoscale*, 2017, **9**, 9562–9571.
21 S. Abdolhosseinzadeh, H. Asgharzadeh and H. Seop Kim, *Sci. Rep.*, 2015, **5**, 10160.
22 J. Zhang, H. Yang, G. Shen, P. Cheng, J. Zhang and S. Guo, *Chem. Commun.*, 2010, **46**, 1112–1114.
23 K. K. H. De Silva, H. H. Huang and M. Yoshimura, *Appl. Surf. Sci.*, 2018, **447**, 338–346.
24 C. Mattevi, G. Eda, S. Agnoli, S. Miller, K. A. Mkhoyan, O. Celik, D. Mastrogiovanni, G. Granozzi, E. Garfunkel and M. Chhowalla, *Adv. Funct. Mater.*, 2009, **19**, 2577–2583.
25 B. L. Kyu Hyung Lee, S.-J. Hwang, J.-U. Lee, H. Cheong, K. S. Oh-Sun Kwon and N. H. Hur, *Carbon*, 2014, **69**, 327–335.
26 S. P. Lee, G. A. M. Ali, H. H. Hegazy, H. N. Lim and K. F. Chong, *Energy Fuels*, 2021, **35**, 4559–4569.
27 C. J. Li and B. M. Trost, *Proc. Natl. Acad. Sci. U. S. A.*, 2008, **105**, 13197–13202.
28 N. D. K. Tu, J. Choi, C. R. Park and H. Kim, *Chem. Mater.*, 2015, **27**, 7362–7369.
29 M. Pelaez-Fernandez, A. Bermejo, A. M. Benito, W. K. Maser and R. Arenal, *Carbon*, 2021, **178**, 477–487.
30 J. P. Jog, *J. Macromol. Sci., Part A: Pure Appl.Chem.*, 1995, **35**, 531–553.
31 V. Ratta, E. J. Stancik, A. Ayambem, H. Pavatareddy, J. E. McGrath and G. L. Wilkes, *Polymer*, 1999, **40**, 1889–1902.
32 W. Chen and L. Yan, *Nanoscale*, 2010, **2**, 559–563.
33 P. V. Kumar, N. M. Bardhan, S. Tongay, J. Wu, A. M. Belcher and J. C. Grossman, *Nat. Chem.*, 2014, **6**, 151–158.
34 C. Mattevi, G. Eda, S. Agnoli, S. Miller, K. A. Mkhoyan, O. Celik, D. Mastrogiovanni, G. Granozzi, E. Garfunkel and M. Chhowalla, *Adv. Funct. Mater.*, 2009, **19**, 2577–2583.
35 O. M. Slobodian, P. M. Lytvyn, A. S. Nikolenko, V. M. Naseka, O. Y. Khyzhun, A. V. Vasin, S. V. Sevostianov and A. N. Nazarov, *Nanoscale Res. Lett.*, 2018, **13**, 139.

 This journal is © The Royal Society of Chemistry 2023

Open Access Article. Published on 16 February 2023. Downloaded on 2/15/2026 5:33:27 PM. This article is licensed under a Creative Commons Attribution 3.0 Unported Licence.

36 H. L. Kuibo Yin, Y. Xia, H. Bi, J. Sun, Z. Liu and L. Sun, *Nano-Micro Lett.*, 2011, **3**, 51–55.
37 B. Xu, S. Yue, Z. Sui, X. Zhang, S. Hou, G. Cao and Y. Yang, *Energy Environ. Sci.*, 2011, **4**, 2826–2830.
38 B. C. Kim, W. J. Cho, W. G. Lee, S. J. Kim, R. Jalili, S. Y. Park, G. G. Wallace, K. H. Yu and S. J. Chang, *Synth. Met.*, 2014, **193**, 110–116.
39 Y. Tian, Z. Yu, L. Cao, X. L. Zhang, C. Sun and D.-W. Wang, *J. Energy Chem.*, 2021, **55**, 323–344.
40 Z. Li, S. Gadipelli, Y. Yang, G. He, J. Guo, J. Li, Y. Lu, C. A. Howard, D. J. L. Brett, I. P. Parkin, F. Li and Z. Guo, *Energy Storage Mater.*, 2019, **17**, 12–21.
41 P. L. B. Zhaoa, Y. Jianga, D. Pana, H. Taob, J. Songa, T. Fanga and W. Xua, *J. Power Sources*, 2012, **198**, 423–427.
42 W. Lv, D. M. Tang, Y. B. He, C.-H. You, Z. Q. Shi, X.-C. Chen, C.-M. Chen, P. X. Hou, C. Liu and Q. H. Yang, *ACS Nano*, 2009, **3**, 3730–3736.
43 C. G. Powell, *American institute of physics handbook*, McGraw-Hill, Dallas, 3rd edn, 1972.
44 W. W. Tyler and A. C. Wilson, *Phys. Rev.*, 1953, **89**, 870–875.
45 H. O. Pierson, *Handbook of Carbon, Graphite, Diamonds and Fullerenes*, 1993.
46 K. Woll, T. Neuhauser, C. Acuña, D. Diaz-Droguett and A. Rosenkranz, *Lubricants*, 2019, **7**, 96.
47 A. Ganguly, S. Sharma, P. Papakonstantinou and J. Hamilton, *J. Phys. Chem. C*, 2011, **115**, 17009–17019.
48 I. A. Vacchi, C. Spinato, J. Raya, A. Bianco and C. Ménard-Moyon, *Nanoscale*, 2016, **8**, 13714–13721.
49 S. Guo, J. Raya, D. Ji, Y. Nishina, C. Ménard-Moyon and A. Bianco, *Nanoscale Adv.*, 2020, **2**, 4085–4092.
50 M. A. Lucherelli, J. Raya, K. F. Edelthalhammer, F. Hauke, A. Hirsch, G. Abellán and A. Bianco, *Chem. – Eur. J.*, 2019, **25**, 13218–13223.
51 I. A. Vacchi, S. Guo, J. Raya, A. Bianco and C. Ménard-Moyon, *Chem. – Eur. J.*, 2020, **26**, 6591–6598.
52 S. Claramunt, A. Varea, D. López-Díaz, M. M. Velázquez, A. Cornet and A. Cirera, *J. Phys. Chem. C*, 2015, **119**, 10123–10129.
53 A. A. K. King, B. R. Davies, N. Noorbehesht, P. Newman, T. L. Church, A. T. Harris, J. M. Razal and A. I. Minett, *Sci. Rep.*, 2016, **6**, 19491.
54 J. B. Wu, M. L. Lin, X. Cong, H. N. Liu and P. H. Tan, *Chem. Soc. Rev.*, 2018, **47**, 1822–1873.
55 A. Y. Lee, K. Yang, N. D. Anh, C. Park, S. M. Lee, T. G. Lee and M. S. Jeong, *Appl. Surf. Sci.*, 2021, **536**, 147990.
56 S. Vollebregt, R. Ishihara, F. D. Tichelaar, Y. Hou and C. I. M. Beenakker, *Carbon*, 2012, **50**, 3542–3554.
57 F. Tuinstra and J. L. Koenig, *Chem. Phys.*, 1970, **53**, 1126–1130.
58 S. Hun, in *In Physics and Applications of Graphene - Experiments*, ed. S. Mikhailov, InTech, 2011, ch. 5, DOI: 10.5772/14156.
59 I. Sengupta, S. Chakraborty, M. Talukdar, S. K. Pal and S. Chakraborty, *J. Mater. Res.*, 2018, **33**, 4113–4122.
60 T. S. Mathis, N. Kurra, X. Wang, D. Pinto, P. Simon and Y. Gogotsi, *Adv. Energy Mater.*, 2019, **9**, 1902007.
61 C. Zhong, Y. Deng, W. Hu, J. Qiao, L. Zhang and J. Zhang, *Chem. Soc. Rev.*, 2015, **44**, 7484–7539.
62 B. Zhao, P. Liu, Y. Jiang, D. Pan, H. Tao, J. Song, T. Fang and W. Xu, *J. Power Sources*, 2012, **198**, 423–427.
63 H. Zhang, V. V. Bhat, N. C. Gallego and C. I. Contescu, *ACS Appl. Mater. Interfaces*, 2012, **4**, 3239–3246.
64 Y. Wang, Z. Shi, Y. Huang, Y. Ma, C. Wang, M. Chen and Y. Chen, *J. Phys. Chem. C*, 2009, **113**, 13103–13107.
65 L. T. Le, M. H. Ervin, H. Qiu, B. E. Fuchs and W. Y. Lee, *Electrochem. Commun.*, 2011, **13**, 355–358.
66 H. Cao, X. Peng, M. Zhao, P. Liu, B. Xu and J. Guo, *RSC Adv.*, 2018, **8**, 2858–2865.
67 Z. Li, S. Gadipelli, Y. Yang and Z. Guo, *Small*, 2017, **13**, 1702474.
68 L. P. Bakos, L. Sárvári, K. László, J. Mizsei, Z. Kónya, G. Halasi, K. Hernádi, A. Szabó, D. Berkesi, I. Bakos and I. M. Szilágyi, *Nanomaterials*, 2020, **10**, 2313.
69 J. Zhao and A. F. Burke, *J. Energy Chem.*, 2021, **59**, 276–291.
70 P. Sinha and K. K. Kar, in *Handbook of Nanocomposite Supercapacitor Materials II: Performance*, ed. K. K. Kar, Springer International Publishing, Cham, 2020, pp. 71–87, DOI: 10.1007/978-3-030-52359-6_3.
71 M. D. Stoller, S. Park, Y. Zhu, J. An and R. S. Ruoff, *Nano Lett.*, 2008, **8**, 3498–3502.
72 E. Frackowiak and F. Béguin, *Carbon*, 2001, **39**, 937–950.
73 D. Pakulski, V. Montes-García, A. Gorczyński, W. Czepa, T. Chudziak, P. Samorì and A. Ciesielski, *J. Mater. Chem. A*, 2022, **10**, 16685–16696.
74 C. Xu, B. Xu, Y. Gu, Z. Xiong, J. Sun and X. S. Zhao, *Energy Environ. Sci.*, 2013, **6**, 1388–1414.
75 J. Raya, A. Bianco and J. Hirschinger, *Phys. Chem. Chem. Phys.*, 2020, **22**, 12209–12227.
76 E. L. Hahn, *Phys. Rev.*, 1950, **80**, 580–594.
77 J. C. C. Freitas, F. G. Emmerich, G. R. C. Cernicchiaro, L. C. Sampaio and T. J. Bonagamba, *Solid State Nucl. Magn. Reson.*, 2001, **20**, 61–73.
78 M. D. Stoller and R. S. Ruoff, *Energy Environ. Sci.*, 2010, **3**, 1294–1301.
79 V. Montes-García, R. F. de Oliveira, Y. Wang, A. Berezin, P. Fanjul-Bolado, M. B. González García, T. M. Hermans, D. Bonifazi, S. Casalini and P. Samorì, *Adv. Funct. Mater.*, 2021, **31**, 2008554.